Elastic rescattering photoelectron distributions entering the relativistic regime

Sui S. Luo, Pat Grugan, Siyu Luo, and Barry C. Walker*

Physics and Astronomy Department, University of Delaware, Newark, DE 19716, USA
*Corresponding author: bcwalker@udel.edu

We report photoelectron energy spectra and angular distributions for ionization with elastic scattering in ultra-strong laser fields. Noble gas species with Hartree–Fock scattering potentials show a reduction in elastic rescattering with the increasing energy of ultrastrong fields and when the Lorentz deflection of the photoelectron exceeds its wave function spread. The relativistic extension of a three-step recollision model is well-suited to the ultrastrong intensity regime ($>10^{17}$ W/cm^2) that lies between traditional strong fields and extreme relativistic interactions.

OCIS codes: 020.2649, 020.4180, 020.0020, 320.0320.
doi: 10.3788/COL201513.070004.

High-strength laser fields can exceed the binding nuclear Coulomb field for atoms and molecules and ionize the outer, least tightly bound electron. Fields of this strength (0.17 a.u., intensities of 10^{15} W/cm^2) dominate photoelectron dynamics and the oscillating laser field can force the photoelectron to return and 'rescatter' with the parent ion[1]. Strong field ionization and rescattering has been used to measure electron dynamics[2], collisionally excite multiple electrons[3], generate coherent attosecond x-ray light[4], and perform molecular tomography[5]. Photoelectron angular distributions are a key to understanding the physics of elastic rescattering in strong laser fields. Collaborative theoretical and experimental efforts[6] disentangled the many possible excitation pathways. These studies clarified the role of the short-range (recollision near the parent ion) and long-range (recollision away from the parent ion core) elastic rescattering.

The three-step model of ionization[7,8] has provided a context by which many strong field processes, including elastic scattering, can be clearly understood. The three-step analysis is traditionally limited to nonrelativistic, dipole interactions where the energy scale of the interaction [e.g., the ponderomotive energy $U_p = e^2|E|^2/(4m\omega^2)$ for an electron charge $-e$ oscillating in an electric field E at a frequency ω] is far less than the electron rest mass m. As the intensity is increased to "ultrastrong" fields[9] nonrelativistic and dipole approximations are no longer accurate. The external magnetic field B can deflect the photoelectron rescattering and cause it to miss the parent ion[10]. The ratio of the Lorentz deflection distance to the spatial width of the returning electron wave is indicated by a Lorentz deflection parameter[11,12], $\Gamma_r = U_p^{3/2}\ V_{IP}/(3c^2\omega)$ for ionization from a binding energy V_{IP}. When $\Gamma_r = 1$, the deflection of the returning electron is equal to its spatial extent. It follows that for $\Gamma_r \gg 1$ rescattering will be reduced to the point of shutdown. At even higher 'extreme' fields[13], relativistic effects, radiation processes, and the external B field affect both bound and continuum electrons.

The purpose of this Letter is to understand the elastic scattering process as it changes from strong to ultrastrong fields. Elastic scattering is a primary mechanism by which the field converts energy into particle motion, a process that is critical to realizing many long-term goals in science including laser fusion. As was the case for pioneering studies in the strong field[14,15], the complexity of the ultrastrong field frontier requires theoretical models than can accurately capture experimental observations. In ultrastrong fields the electron can quickly become relativistic and traverse a large portion, or even exit, the laser focus during a femtosecond laser pulse. Spatial and temporal integration of the interaction region can be an integral part of understanding the forces experienced by the photoelectron on the way to the detector and the science that underlies the measurements[16]. We report on the photoelectron angular distributions from Ne, Ar, and Xe across strong and ultrastrong fields. The results show how the Lorentz deflection affects the rescattering and can reduce it to a negligible level as one advances into the ultrastrong field regime. Comparisons of these angular distributions to future experiments will be needed to quantify whether several assumptions in the models are correct, such as a lack of multielectron excitation. The flexibility of the model should allow for valid elastic scattering calculations with most atoms and ions at field interactions where $\Gamma_r \sim 1$ and the interaction is not yet into the extreme relativistic regime[13].

The model used represents an emerging technique that accurately captures ultrastrong field physics. Interactions (such as ionization[17] or radiation reaction[18]) are treated quantum mechanically and propagation in the field is handled classically when the electron deBroglie wavelength is much smaller than the drive wavelength. Properly applied the technique has advantages in its extension physically of the three step model[7] to ultrastrong fields and insight from its intuitive treatment of ionization, propagation, and recollision. The full reasons behind

the validity of this three-step parsing are complex but lie within the different approximations valid for each step. For the first step of tunneling ionization, the energy scales are of order 10 to 30 a.u. While the external field does affect the ionizing bound state near the nucleus, it does not generally change the bound state wave function or ionization rate by more than a factor of 2[19,20]. In this study, we use the low-frequency, nonrelativistic tunneling ionization rate[17] also referred to as the Ammosov, Delone, Krainov rate[21]. The electric field in the studies is a $\sigma = 34$ fs pulsed, $\lambda = 800$ nm carrier wavelength, plane wave,

$$\boldsymbol{E} = E_0 \sin(2\pi/\lambda\ z - \omega t) \exp\left(-\left(t - \frac{z}{c}\right)^2 / \sigma^2\right)\hat{\mathbf{x}}. \quad (1)$$

When considering the full field, $\boldsymbol{B} = |\boldsymbol{E}|/c\hat{\mathbf{y}}$, where $\hat{\mathbf{x}}, \hat{\mathbf{y}}, \hat{\mathbf{z}}$ are the unit vectors in cartesian coordinates. In the dipole approximation we set $\boldsymbol{B} = 0$. For all the results presented in this Letter we adjust E_0 such that the atom or ion has reached 90% ionization by the end of the pulse.

In the second step, the external field accelerates the electron to energies that can exceed 10^3 Hartree. Quantum aspects in the continuum are arguably captured using a Monte Carlo trajectory ensemble with uncertainties in momentum and position determined by tunneling ionization. The semiclassical trajectory ensemble method used has been described previously[22]. Briefly, for each time step we propagate on the order of 10^4 trajectories with a weight determined by the ionization to represent the quantum photoelectron in the continuum. The trajectories are generated by integrating Hamilton's equations of motion with the external field $\boldsymbol{E}$ and soft core ion potential ($\delta \sim 0.2$)

$$\frac{dp_x}{dt} = \frac{-Z\ \mathrm{e}^2 x}{(r^2 + \delta)^{3/2}} - \mathrm{e}|\boldsymbol{E}|\left[1 - \frac{p_z}{\sqrt{p^2 + m^2 c^2}}\right], \quad (2)$$

$$\frac{dp_y}{dt} = \frac{-Z\ \mathrm{e}^2 y}{(r^2 + \delta)^{3/2}}, \quad (3)$$

$$\frac{dp_z}{dt} = \frac{-Z\ \mathrm{e}^2 z}{(r^2 + \delta)^{3/2}} - \mathrm{e}|\boldsymbol{E}|\frac{p_x}{\sqrt{p^2 + m^2 c^2}}, \quad (4)$$

$$\frac{dx}{dt} = \frac{p_x c}{\sqrt{p^2 + m^2 c^2}}, \quad (5)$$

$$\frac{dy}{dt} = \frac{p_y c}{\sqrt{p^2 + m^2 c^2}}, \quad (6)$$

$$\frac{dz}{dt} = \frac{p_z\ c}{\sqrt{p^2 + m^2 c^2}}, \quad (7)$$

where p_x, p_y, p_z are the momenta along the cartesian coordinates; Z is the ion charge and t is time. An example snapshot of a trajectory ensemble from ionization just after the peak of the optical cycle at an intensity of 1.3×10^{17} W/cm^2 is shown in Fig. 1. In Fig. 1 we follow an
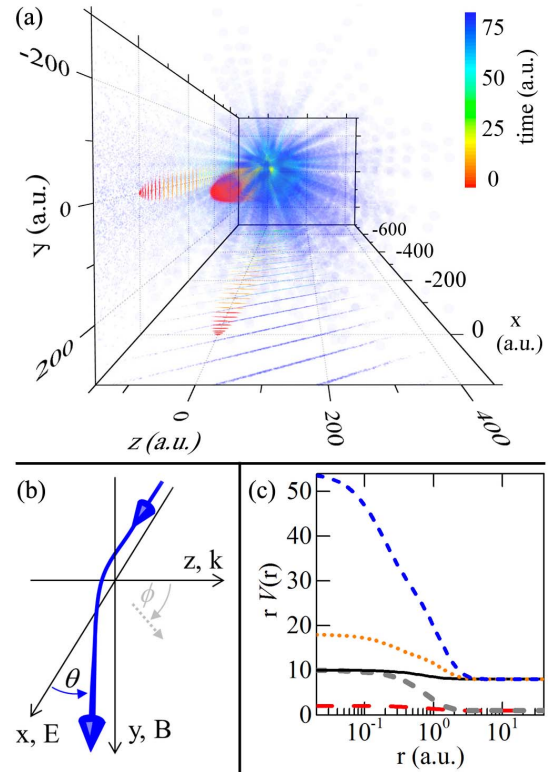

Fig. 1. Monte Carlo ensemble for 10^3 trajectories: (a) from ionization at an intensity of 1.3×10^{17} W/cm^2 and its return to the core 70 a.u. later. Symbol is plotted for every 1.1 a.u. time step from ionization at $t = 0$. Color mapping used for propagation time after ionization. The XZ- and XY-plane projections show the rapid spreading of the electron from ionization at the origin. In addition, the increasing distance between the 1.1 a.u. time steps in the plane projections indicate the electron acceleration in the field and the tilt of the electron wave front from the Lorentz force (XZ-projection); (b) coordinate system for the elastic scattering from the nucleus shown in (a); (c) scattering potentials for Ne$^+$, Ne^{8+}, Ar^{8+}, and Xe^{8+}. Atomic units (a.u.) are used.

example of 1000 trajectories for ionization at $z = 0$, $t = -188$ a.u. in a pulse with a peak intensity of 1.3×10^{17} W/cm^2 (i.e., $\boldsymbol{E} = -1.7\,\hat{\mathbf{x}}$ in atomic units) to the return at $z = 0$, $t = -118$ a.u., ($\boldsymbol{E} = 0.6\,\hat{\mathbf{x}}$). The rapid spreading of the initial ionization is clear in Fig. 1 as well as the Lorentz deflection of the photoelectron by approximately 50 a.u. in the direction of z when it returns 70 a.u. of time later. For this case ($\Gamma_r = 3.2$), the resulting rescattering flux that revisits the core is 4% of the peak value [i.e., $\exp(-3.2)$]. Fortunately, to a high level of accuracy, the returning electron can be treated as a plane wave since the rescattering electron wave at ~200 a.u. wide is much larger that the ~1 a.u. length scale of the scattering potential.

Upon the return of the photoelectron to the core, we calculate elastic scattering with the parent ion. Elastic scattering in ultrastrong fields is affected by new aspects when compared with scattering in strong fields. The Lorentz deflection in the continuum, as ionization is driven by the external field, is addressed by the trajectory

ensemble method described previously. The relativistic continuum and rescattering process with the ion potential must be treated accurately since ultrastrong fields present large recollision energies; scattering probes effective charges very near the full nuclear charge. The potentials used were calculated in the Hartree–Fock approximation using ELSEPA[23]. For clarity, we plot in Fig. 1(c) the potentials' effective charge, i.e., $rV(r)$, as a function of distance from the nucleus. Viewed in this way, one can more easily see the screening provided by the ion core. After elastic scattering the photoelectron continues to interact with the field until the laser pulse has passed, typically two pulse durations (2σ) after the peak.

We display the calculated final photoelectron energy spectrum in Fig. 2. The angle integrated photoelectron yields for Ne+, Xe8+, Ar8+, and Ne8+ are plotted for nonrelativistic, dipole calculations, and full fields with relativity. For ease of comparison, energy units of U_p were chosen in Fig. 2. We present the scattering normalized to the amount of ionization, i.e., the integration of the photoelectron energy spectrum over energy gives a value of 1. We begin with Ne+, which can be compared to experiments in the strong field[24]. The yield shows the characteristic low energy ionization from 0 to $2U_p$ and the high energy plateau from rescattering with the parent ion that stretches from $2U_p$ to $10U_p$[8]. There is, as expected, no difference between the nonrelativistic dipole calculations and those including relativity and the B field for Ne+. Figure 2 also displays ionization for Xe8+ at 2×10^{16} W/cm², Ar8+ at 5×10^{16} W/cm², and Ne8+ at 3×10^{17} W/cm². These species extend into the ultrastrong field and two primary factors are responsible for the decrease in rescattering as the intensity increases. The first, as in Rutherford scattering, is the inverse square energy dependence of the scattering process. Since the
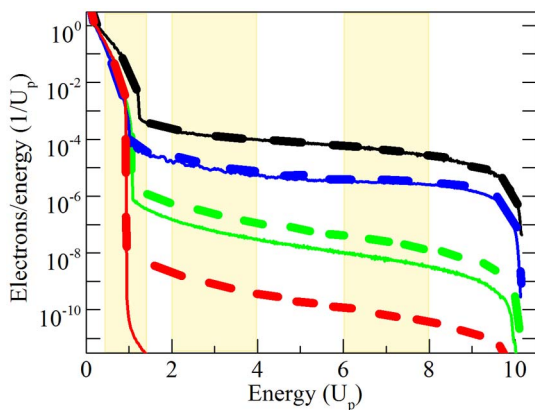
recollision energy (i.e., U_p) scales with the intensity, one can expect a quadratic drop in the scattering yield with increasing intensity. The second is the Lorentz deflection shown in Fig. 1. The decrease in electron yield from $2U_p$ to $10U_p$ for Xe8+ is a result of the energy dependence of elastic scattering. Despite the large nuclear charge for xenon, the higher intensity decreases the elastic scattering yield by 1 order of magnitude compared to Ne+. The ionization of Ar8+ occurs at a $\Gamma_r = 1$ so the expected reduction from the Lorentz factor is 0.37, i.e., $\exp(-\Gamma_r)$. Nevertheless, comparing the nonrelativistic, dipole calculation for Ar8+ to the relativistic full field result shows in this case, the nearly 3 order of magnitude drop in rescattering compared to Ne+ is due primarily to the higher energies in ultrastrong fields. Progressing to Ne8+ at 3×10^{17} W/cm², the mechanism behind the reduction in the rescattering changes abruptly to Lorentz deflection. For Ne8+ the Lorentz deflection parameter is $\Gamma_r = 15.6$. The new role of the Lorentz reduction in rescattering can be clearly seen in Fig. 2. While the intensity has increased only by a factor of 6 from Ar8+ to Ne8+ (5×10^{16} W/cm² to 3×10^{17} W/cm²) the rescattering in Ne8+ is absent at a level of 10^{-11} of the photoionization yield.

In Fig. 3 we show the calculated angular distributions at the photoelectron energies (±energy integration range) of $U_p(\pm 0.5U_p)$, $3U_p(\pm U_p)$, and $7U_p(\pm U_p)$ in the nonrelativistic, dipole case [Figs. 3(a)–3(c)] and in the fully relativistic case with the laser magnetic field [Figs. 3(d)–3(f)]. The authors note the relativistic, B field yields for Ne8+ are vanishingly small and do not appear in Fig. 2. For reference, these are for Ne8+ at $3U_p$, 6.1×10^{-14} electrons/energy $(1/U_p)$, and at $7U_p$, 4.8×10^{-19} electrons/energy $(1/U_p)$. The angular distributions are presented as an angle θ from the electric field axis (Fig. 1). We plot the different species together to better understand the contributing mechanisms and expected changes in the angular distributions going into the ultrastrong field. All yields are normalized to aid in comparison.
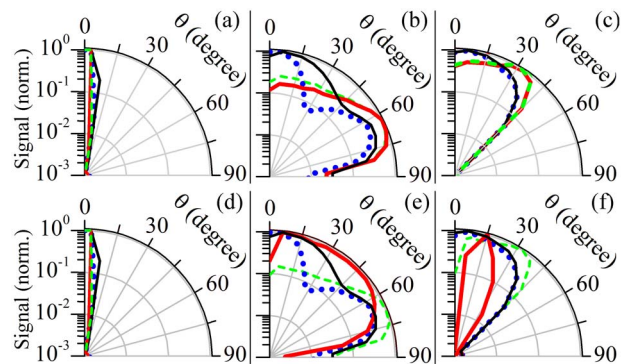

Fig. 2. Angle-integrated photoelectron energy distributions for Ne+ (black, $U_p = 2.6$ a.u.), Xe8+ (blue, $U_p = 38$ a.u.), Ar8+ (green, $U_p = 115$ a.u.), and Ne8+ (red, $U_p = 770$ a.u.) as a function of the final photoelectron energy. Yield is given in electrons per unit U_p energy. For each species, we show the nonrelativistic dipole (thick, dash) and the relativistic full field (solid) yields. Energy integration regions for the angular distributions shown in Fig. 3 are highlighted.

Fig. 3. Photoelectron angular distributions calculated for B = 0, for Ne+ (solid, black), Xe8+ (dotted, blue), Ar8+ (dash, green), and Ne8+ (thick solid, red): (a)–(c) nonrelativistically; (d)–(f) full field, relativistically; (a), (d) for energies $U_p \pm 0.5U_p$; (b), (e) for energies $3U_p \pm U_p$; and (c), (f) for energies $7U_p \pm U_p$. Yields are normalized to the peak value at that energy (Fig. 2).

One may retrieve the actual yield at any energy for these species by combining the angular distribution with the angle integrated results of Fig. 2.

Ionization at energies of U_p in Figs 3(a) and 3(c) have an angular emission, $\theta = \arctan((p_y^2 + p_z^2)^{1/2}/p_x)$, that is dominated by the initial momentum from ionization and drift energy from the field without scattering. The angular width is narrow ($\theta < 15°$) for ionization by a plane wave. Due to the acceleration and momentum along the laser field direction, p_x increases quickly when going to ultrastrong fields. Since the transverse momentum (p_y, p_z) determined by the atomic bound state does not change by more than a factor of 3 across these species, the distributions become more aligned with the field as one proceeds from Ne^+ to Xe^{8+} to Ar^{8+} to Ne^{8+}.

As one increases to $3U_p$, rescattering is the mechanism behind the yield and the emission angle for all the species is at its broadest extending from 0° to 90° from the laser electric field. The combination of the returning energy and scattering potential gives the observed structure and 'scattering rings' at large angles first observed in xenon[25]. What is important to observe from Figs. 3(b) and 3(e) is the B field and relativistic effects do not change the angular distribution until one is well into the $\Gamma_r \gg 1$ regime where Lorentz deflection has greatly reduced the yield. For Ar^{8+}, where $\Gamma_r \cong 1$, there is no significant difference in the angular distributions of Figs. 3(b) and 3(d). Proceeding to the highest energy, $7U_p$ distributions in Fig. 3(c), the angular emission range narrows as the mechanism changes over to backscattering into narrow angles along the electric field. The smaller impact parameters for the scattering process give these higher energies a greater sensitivity to the Lorentz deflection. In Figs. 3(c) and 3(f), one can see backscattering ($\theta = 0$) for both Ar^{8+} and Ne^{8+} is lower in Fig. 3(f) with the external laser B field compared to Fig. 3(c).

As the intensity increases, the Lorentz deflection that increases Γ_r and causes the rescattering electron to miss the parent ion also forward-deflects the overall photoionization yield[22]. In a plane wave this forward deflection is described by[26].

$$\tan \theta = \sqrt{2mc^2/E_{\text{kinetic}}}. \tag{8}$$

At intensities of 3×10^{17} W/cm^2 and below, this is not a concern in our context for the angular distributions since the forward-deflection angle from this field momentum is less than 5°.

In conclusion, we use a relativistic extension of a three-step recollision model with Hartree–Fock scattering potentials to calculate photoelectron energy spectra and angular distributions for ionization with elastic scattering from strong to ultrastrong fields up to 3×10^{17} W/cm^2. The yield of the noble gas species shows a decrease in the rescattering yield due to the inverse square dependence of the elastic scattering on energy. As the laser magnetic field affects the photoionization, there is an sharp reduction in elastic rescattering when $\Gamma_r > 1$. The onset of the reduction from 5×10^{16} to 3×10^{17} W/cm^2 decreases the rescattering yield by $\sim 10^5$ over a change of intensity by a factor of 6. The angular distributions of the photoelectrons are not drastically changed during the range $0 < \Gamma_r < 1$. For $\Gamma_r > 1$, elastic backscattering at large energies is most strongly effected, corresponding to short-range collisions between the parent ion and the returning photoelectron. The relativistic extension of a three-step recollision model with accurate atomic potentials is well-suited to comparison with experiments in the ultrastrong intensity regime that lies between traditional strong fields and extreme relativistic interactions.

References

1. L. F. DiMauro and P. Agostini, Adv. At. Mol. Opt. Phys. D **35**, 79 (1995).
2. Y. Huismans, A. Rouzee, A. Gijsbertsen, J. H. Jungmann, A. S. Smolkowska, P. S. W. M. Logman, F. Lepine, C. Cauchy, S. Zamith, T. Marchenko, J. M. Bakker, G. Berden, B. Redlich, A. F. G. van der Meer, H. G. Muller, W. Vermin, K. J. Schafer, M. Spanner, M. Y. Ivanov, O. Smirnova, D. Bauer, S. V. Popruzhenko, and M. J. J. Vrakking, Science **331**, 61 (2011).
3. T. Weber, H. Giessen, M. Weckenbrock, G. Urbasch, A. Staudte, L. Spielberger, O. Jagutzki, V. Mergel, M. Vollmer, and R. Dorner, Nature **405**, 658 (2000).
4. M.-C. Chen, C. Mancuso, C. Hernandez-Garcia, F. Dollar, B. Galloway, D. Popmintchev, P.-C. Huang, B. Walker, L. Plaja, A. A. Jaron-Becker, A. Becker, M. M. Murnane, H. C. Kapteyn, and T. Popmintchev, in Proc. Natl. Acad. Sci. USA **111**, E2361 (2014).
5. J. Itatani, J. Levesque, D. Zeidler, H. Niikura, H. Pepin, J. Kieer, P. Corkum, and D. Villeneuve, Nature **432**, 867 (2004).
6. B. Walker, B. Sheehy, K. C. Kulander, and L. F. DiMauro, Phys. Rev. Lett. **77**, 5031 (1996).
7. P. B. Corkum, Phys. Rev. Lett. **71**, 1994 (1993).
8. D. B. Milosevic, G. G. Paulus, D. Bauer, and W. Becker, J. Phys. B **39**, R203 (2006).
9. C. J. Joachain, N. J. Kylstra, and R. M. Potvliege, J. Mod. Opt. **50**, 313 (2003).
10. D. B. Milošević, S. Hu, and W. Becker, Phys. Rev. A **63**, 011403(R) (2000).
11. S. Palaniyappan, I. Ghebregziabher, A. DiChiara, J. MacDonald, and B. C. Walker, Phys. Rev. A **74**, 033403 (2006).
12. M. W. Walser, C. H. Keitel, A. Scrinzi, and T. Brabec, Phys. Rev. Lett. **85**, 5082 (2000).
13. A. Di Piazza, C. Muller, K. Z. Hatsagortsyan, and C. H. Keitel, Rev. Mod. Phys. **84**, 1177 (2012).
14. M. Lewenstein, P. Balcou, M. Y. Ivanov, A. L'Huillier, and P. B. Corkum, Phys. Rev. A **49**, 2117 (1994).
15. B. Walker, B. Sheehy, L. F. Dimauro, P. Agostini, K. J. Schafer, and K. C. Kulander, Phys. Rev. Lett. **73**, 1227 (1994).
16. I. Ghebregziabher and B. C. Walker, Phys. Rev. A **76**, 023415 (2007).
17. V. S. Popov, Phys. Usp. **47**, 855 (2004).
18. J. X. Li, K. Z. Hatsagortsyan, and C. H. Keitel, Phys. Rev. Lett. **113**, 044801 (2014).
19. H. Bauke, H. G. Hetzheim, G. R. Mocken, M. Ruf, and C. H. Keitel, Phys. Rev. A **83**, 063414 (2011).

20. P. D. Grugan, S. Luo, M. Videtto, C. Mancuso, and B. C. Walker, Phys. Rev. A **85**, 053407 (2012).

21. M. V. Ammosov, N. B. Delone, and V. P. Krainov, Zh. Eksperimentalnoi I Teoreticheskoi Fiziki **91**, 2008 (1986).

22. N. Ekanayake, S. Luo, P. D. Grugan, W. B. Crosby, A. D. Camilo, C. V. McCowan, R. Scalzi, A. Tramontozzi, L. E. Howard, S. J. Wells, C. Mancuso, T. Stanev, M. F. Decamp, and B. C. Walker, Phys. Rev. Lett. **110**, 203003 (2013).

23. F. Salvat, A. Jablonski, and C. J. Powell, Comput. Phys. Commun. **165**, 157 (2005).

24. B. Sheehy, R. Lafon, M. Widmer, B. Walker, L. F. DiMauro, P. A. Agostini, and K. C. Kulander, Phys. Rev. A **58**, 3942 (1998).

25. B. Yang, K. J. Schafer, B. Walker, K. C. Kulander, P. Agostini, and L. F. DiMauro, Phys. Rev. Lett. **71**, 3770 (1993).

26. C. I. Moore, A. Ting, S. J. McNaught, J. Qiu, H. R. Burris, and P. Sprangle, Phys. Rev. Lett. **82**, 1173 (1999).